Characterization of Hydrogenated Amorphous Silicon Detectors With Clinical Photon and Electron Beams

M. Ponzecchi, K. Kanxheri, L. Servoli, M. V. Rossi, E. Gazzera, G. Insero, S. Pallotta, M. Fabi, C. Grimani, F. Sabbatini, M. Villani, S. Aziz, L. Calcagnile, A. P. Caricato, M. Martino, G. Maruccio, A. G. Monteduro, G. Quarta, S. Rizzato, R. Catalano, G. A. P. Cirrone, G. Cuttone, M. Guarrera, G. Petringa, L. Frontini, V. Liberali, A. Stabile, M. M. S. Vasquez, F. Cittadini, T. Croci, M. Ionica, M. Menichelli, A. Morozzi, *Member, IEEE*, D. Passeri, *Senior Member, IEEE*, M. Pedio, F. Peverini, P. Placidi, *Senior Member, IEEE*, N. Zema, D. Caputo, *Member, IEEE*, G. de Cesare, *Member, IEEE*, N. Lovecchio, *Member, IEEE*, A. Nascetti, *Member, IEEE*, M. Cazzanelli, H. Hasnaoui, M. Polo, A. Quaranta, D. Calvo, R. Cirio, P. De Remigis, F. Lenta, G. Mazza, *Member, IEEE*, R. J. Wheadon, S. Dunand, G. Konstantinou, N. Wyrsch, L. Barraud, A. Bashiri, M. Large, M. Petasecca, *Member, IEEE*, and C. Talamonti

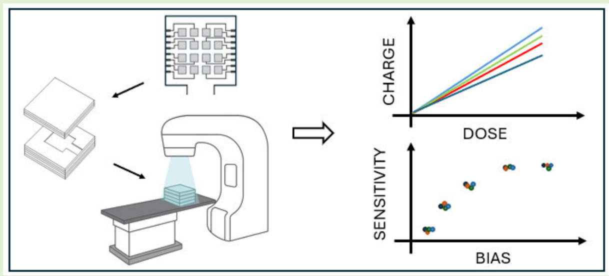

***Abstract*—Flexible hydrogenated amorphous silicon (a-Si:H) detectors are attractive candidates for clinical dosimetry, particularly for applications requiring lightweight devices and operation without external bias. In this work, three flexible a-Si:H detector architectures are experimentally compared under clinical photon and electron beams: a conventional n-i-p diode, a charge selective contact (CSC) detector, and a very thin p-i-n diode. All detectors show excellent dose linearity under both irradiation modalities. However, large differences in sensitivity are observed at zero bias, exceeding two orders of magnitude across architectures. The conventional n-i-p device shows a response that is limited by the internal electric field, while CSC and very thin p-i-n detectors achieve sensitivities in the pC/cGy range without applied bias. Electron beams yield higher charge per unit dose than photons, compatible with a larger local energy deposition in the active layer. The results demonstrate that sensitivity in flexible a-Si:H dosimeters is governed by contact design and intrinsic layer thickness rather than by active volume alone. Taken together, the present results suggest that combining CSCs with thinner intrinsic layers may represent a promising strategy to further enhance zero-bias sensitivity. These findings provide clear design guidelines for the development of flexible dosimeters for surface and transmission measurements in advanced radiotherapy (RT).**

***Index Terms*—Charge selective contact (CSC) detector, hydrogenated amorphous silicon (a-Si:H), p-i-n detector, sensitivity.**

I. Introduction

RADIOTHERAPY (RT) is a cornerstone of cancer management. Advances in engineering, materials science, and computational methods over the past few decades have directly influenced RT techniques [1]. Innovative treatments such as intensity-modulated radiation therapy (IMRT), volumetric modulated arc therapy (VMAT), and emerging FLASH therapy have improved dose conformity, enabling smaller planning margins and higher prescription doses. These technological advances impose stringent requirements on dosimetry, demanding accurate real-time measurements at very high dose rates. Standard dosimeters, including ionization chambers and solid-state devices, remain reliable and widely used in conventional RT but are constrained by their fixed geometries and limited adaptability and, in some cases, by reduced sensitivity or performance degradation under very high-dose-rate irradiation. Overcoming these limitations requires new detector technologies combining high sensitivity, fast response, radiation tolerance,

Received 11 March 2026; accepted 22 April 2026. Date of publication 7 May 2026; date of current version 16 June 2026. This work was supported in part by the Hydrogenated Amorphous Silicon Pixels Detectors (HASPIDE) Project funded by Istituto Nazionale di Fisica Nucleare (INFN) through the CSN5, Dosimetric Characterization of Detectors and Particle Beams at Ultra-High Dose Rates in Radiotherapy (PANDORA) Project [PNRR, Missione 4, Componente 2 1.5, Finanziata dall'UE—NextGenerationEU, Bando Ministero dell'Università e della Ricerca (MUR) 3277/2021, THE: ECS-00000017, Codice Unico di Progetto (CUP) B83C2200393000], and in part by Swiss National Science Foundation under Grant 200021_212208/1. The associate editor coordinating the review of this article and approving it for publication was Dr. Juan A. Lenero-Bardallo. *(M. Ponzecchi and K. Kanxheri are co-first authors.) (Corresponding authors: L. Servoli; C. Talamonti.)*

Please see the Acknowledgment section of this article for the author affiliations.

Digital Object Identifier 10.1109/JSEN.2026.3689750

and flexible form factors suitable for emerging clinical scenarios.

In this context, the HASPIDE project, funded by INFN, has focused on developing flexible hydrogenated amorphous silicon (a-Si:H) detectors on polymer substrates. Compared to crystalline silicon, a-Si:H exhibits a wider bandgap, intrinsic radiation hardness, and the capability to be deposited at low temperature in thin and uniform layers over large-area and mechanically flexible substrates [2], [3]. These features enable the realization of lightweight, conformable, and wearable detectors, making a-Si:H a particularly attractive candidate for next-generation dosimetry systems.

Despite these advantages, the optimization of flexible a-Si:H detectors for clinical dosimetry remains an open technological and physical challenge. In a-Si:H devices, detector sensitivity is not governed solely by the sensitive volume but is strongly influenced by carrier transport, trapping, and recombination processes, as well as by the internal electric field distribution across the intrinsic layer [4], [5]. These factors depend critically on both the intrinsic layer thickness and the nature of the contacts. Conventional p-i-n and n-i-p structures rely on heavily doped layers, which can introduce a high density of defect states at the interfaces and limit carrier lifetime and collection efficiency [5]. More recently, charge selective contacts (CSCs) based on transition metal oxides have been proposed to enhance built-in electric fields and suppress interfacial recombination, enabling more efficient charge extraction even when operating at zero bias [6], [7].

A systematic experimental comparison of these different flexible device architectures under realistic clinical radiation beams is still lacking. Therefore, in this work, we present a comparative characterization of three flexible a-Si:H detector architectures fabricated on Kapton substrates: a conventional n-i-p diode, an ultrathin p-i-n diode, and a CSC device. The detectors were tested under clinical photon and electron beams produced by a medical linear accelerator (linac). Their response was investigated in terms of dose linearity, sensitivity, pixel uniformity, and, for the n-i-p device, the effect of external bias. By directly comparing detector architectures with different intrinsic layer thicknesses and contact configurations, this study aims to clarify the physical and technological factors that govern sensitivity at zero bias in flexible a-Si:H dosimeters and to provide design guidelines for future detector development.

II. Materials and Methods

A. Detectors

1) Fabrication Process of Flexible a-Si:H Detectors: The devices were fabricated at two institutions involved in the HASPIDE project: the n-i-p and CSC detectors were manufactured at the Photovoltaics and Thin Film Electronics Laboratory (PV-Lab), EPFL, Neuchâtel, Switzerland, while the p-i-n device was produced at the Department of Information, Electronics, and Telecommunications Engineering, University of Rome La Sapienza, Italy.

All detectors exhibit a vertical structure and are fabricated on Kapton substrates with the bottom Cr/Al/Cr electrode deposited by thermal evaporation (see Fig. 1). The a-Si:H stacks are deposited by plasma-enhanced chemical vapor deposition (PECVD) at 200 °C from hydrogen-diluted silane.

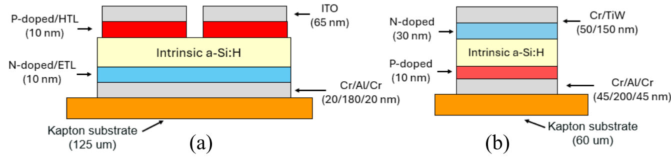

Fig. 1. Structure of the n-i-p/CSC (a) and p-i-n (b) diodes.

In all architectures considered here, the active device is fabricated directly on the flexible Kapton substrate; therefore, no postfabrication transfer step to the printed circuit board (PCB) is involved.

For the n-i-p device, the n-doped a-Si:H layer was obtained by adding phosphine (PH_3) to the gas mixture, while the p-doped a-Si:H layer was deposited using trimethylboron (TMB) as dopant precursor. The top contact consists of a patterned indium tin oxide (ITO) layer deposited by sputtering at room temperature. To minimize peripheral effects and reduce leakage currents, the p-layer around the ITO contact was selectively dry-etched using the ITO itself as a hard mask. Each pixel is connected to a microbonding pad through a copper wire and graphite-based epoxy glue (MG Chemicals 838AR), and to protect the electrical contacts, a 70-μm Kapton tape layer is positioned above the pixels.

For the CSC device, the doped layers were replaced by dopant-free CSCs. In particular, the n-layer was substituted by a titanium dioxide (TiO_2) electron transport layer (ETL) and the p-layer by a molybdenum oxide (MoO_x) hole transport layer (HTL), both deposited by sputtering at room temperature. In this configuration, no peripheral etching was required due to the intrinsically low lateral conductivity of MoO_x. The detector has the same metallic contacts as the n-i-p device. Each pixel is coupled to a microbonding pad with copper wire and silver-based conductive paint.

The p-i-n detector was fabricated using a microelectronic process based on four photolithographic masks. The n- and p-doped layers were formed by introducing PH_3 and diborane (B_2H_6) into the gas mixture, respectively. A thin Cr layer was evaporated to protect the p-i-n-junction and ensure ohmic contact. The sensor geometry was defined by photolithographic patterning of both metal and semiconductor layers, and a negative photoresist (SU-8) was used for passivation and via definition. Finally, a TiW top electrode was deposited by magnetron sputtering [8].

Notably, the fabrication process has evolved over time: the n-i-p diodes belong to an earlier production series, whereas the CSC and p-i-n devices are part of more recent technological developments aimed at improving charge collection efficiency and zero-bias performance.

2) Detector Architectures and Layouts: The characteristics of the a-Si:H detectors are reported in the following.

1) *n-i-p Detector:* (see Fig. 2) Consists of a linear array of five individual diode pixels, spaced at a 5-mm pitch. Each pixel has an intrinsic layer thickness of 2.5 μm and an active area of 2.5 $\times$ 2.5 mm.
2) *CSC Detector:* (see Fig. 3) Comprises a 3 $\times$ 3 matrix of 5 $\times$ 5 mm pixels (6 mm pitch) and a 1 $\times$ 5 array of 2 $\times$ 2 mm pixels (4 mm pitch). In this device, the active region of each pixel is 5 μm thick.

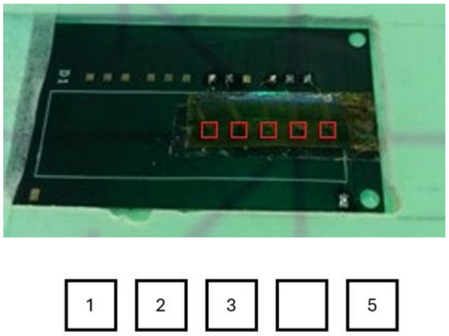

Fig. 2. Upper image shows the n-i-p detector, with pixel edges marked in red; the bottom one presents a schematic view of the pixels with their numerical identifiers used for the data acquisitions.

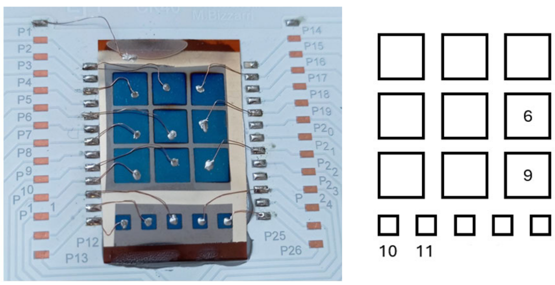

Fig. 3. Left image shows the CSC detector; the right one displays a schematic with numerical identifiers of the pixels used for the measurements.

3) *p-i-n Detector:* (see Fig. 4) Consists of 32 pixels of 2×2 mm, spaced at a 5-mm pitch, with an ultrathin intrinsic layer thickness of 0.4 μm.

Each detector is equipped with a Kapton tail (35 cm long and 400 μm thick) that carries the conductive lines for signal transmission, simplifying the connection to the readout electronics and enabling real-time acquisition of pixel data.

3) Pixel Selection: Each detector comprises multiple pixels, not all of which are suitable for dosimetric characterization. Prior to irradiation tests, all pixels were electrically characterized. Only pixels exhibiting stable dark current, low noise, and reliable electrical connections were selected for measurements. Pixels affected by excessive leakage current, unstable response, or contact failures were excluded.

The reported results, therefore, refer to subsets of pixels meeting predefined performance criteria. The number and identifiers of the pixels used in the measurements are indicated in Figs. 2–4.

B. Irradiation Beams and Clinical Conditions

1) Irradiation Beams: All detector characterization measurements were conducted using the Elekta Versa HD linac located at Careggi University Hospital in Florence (see Fig. 5). Three distinct beam configurations were employed to assess detector performance across different dose rates and temporal structures: flattening filter (FF) photon beams, FF free (FFF) photon beams, and electron beams. Details about the beam's temporal structure can be found in [9], [10], and [11]. The following beams and settings were used for the measurements.

1) *FF Photon Beam:* Standard 6- and 10-MV photon beams were used, varying the dose from 2 to 200 cGy with a nominal dose rate of 500 cGy/min. These conditions were selected to test the detectors across typical clinical doses.
2) *FFF Photon Beam:* An FFF 6-MV photon beam was also employed to conduct dose measurements, ranging from 2 to 200 cGy, with a nominal dose rate of 500 cGy/min. Additional acquisitions were carried out at dose rates between 104 and 1691 cGy/min, using a fixed delivered dose of 200 cGy. Due to the absence of the FF, FFF beams exhibit more intense and temporally sharper pulses. These conditions enabled the evaluation of detector behavior in very high dose rate scenarios relevant for modern stereotactic and hypofractionated RT protocols.
3) *Electron Beam:* In addition to photon beams, 6- and 8-MeV electron beams were used. The dose rate was varied from 38 to 591 cGy/min and from 35 to 645 cGy/min for the 6- and 8-MeV beams, respectively. Electrons offer different energy deposition characteristics and shallower penetration depths, making them suitable for evaluating sensitivity, signal shape, and linearity under distinct irradiation conditions.

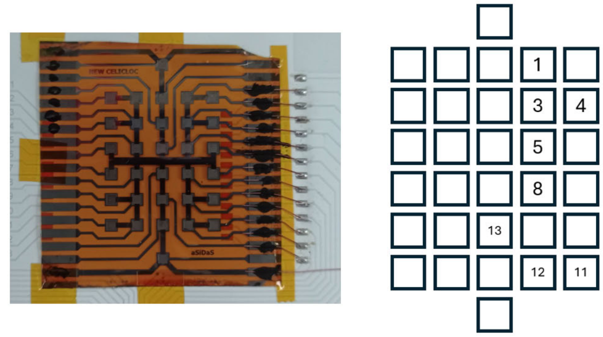

Fig. 4. Left image shows the p-i-n detector; the right one displays a schematic with numerical identifiers of the pixels used for the data acquisitions.

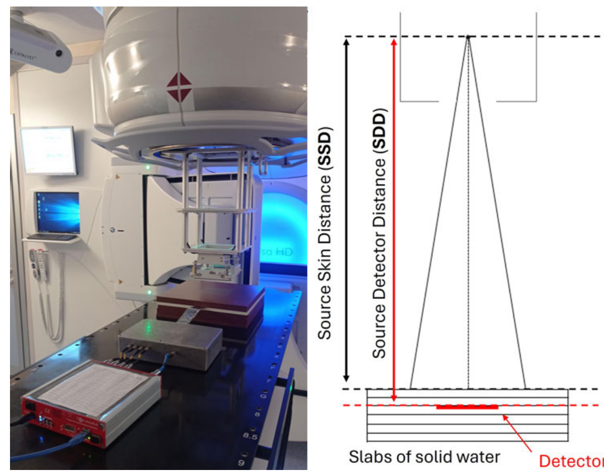

Fig. 5. On the left, the Medical linac Elekta Versa HD at Careggi University Hospital in Florence is shown. The TetrAMM readout electronics (red–gray box) and the interface board (mid-gray box) are placed on the treatment couch. For a proper dosimetric measurement, the detectors are inserted between slabs of solid water. On the right, a schematic of the experimental setup is represented.

2) Experimental Setup: During the acquisitions, all detectors were embedded in solid water slabs to simulate tissue equivalent conditions. Each device was placed in a custom-carved cavity to ensure stable positioning. At least 5 cm of solid water was placed beneath the detectors to ensure adequate backscatter conditions.

Measurements were performed under reference conditions, defined by a field size of 10 × 10 cm, with the detectors positioned at the depth of maximum dose within the solid water slabs. This field size was chosen to ensure that all pixels were located within the uniform region of the beam.

For photon beams, the source-to-detector distance (SDD) was set to 100 cm, while, for electron beams, the source-to-surface distance (SSD), defined here as the distance to the upper surface of the top slab, was set to 100 cm.

The Elekta Versa HD linac was calibrated according to the IAEA TRS-398 protocol [12], using PTW ionization chambers: a PTW 30013 thimble chamber for photon beams and a PTW 34045 plane parallel chamber for electron beams.

C. Readout Electronics

Two readout systems were used to acquire signals from the detectors, chosen to meet different measurement requirements in terms of temporal resolution and signal integration. A multichannel electrometer developed at the Center of Medical Radiation Physics at the University of Wollongong (UOW), Australia, was used for the n-i-p detector. This custom-built system supports simultaneous acquisition from up to six channels and allows adjustable sampling intervals down to about 0.16 ms [13]. This temporal resolution is suitable for dose measurements integrated over acquisition windows that include multiple beam pulses, without resolving their individual time structure.

In contrast, the CSC and p-i-n detectors were read out using the commercial TetrAMM picoammeter (CAEN), a four-channel electrometer with a programmable bias voltage [14]. The TetrAMM system provides a higher temporal resolution, with a minimum sampling period of 10 μs, enabling detailed time-resolved studies of the signal and the temporal structure of pulsed radiation beams. At this acquisition rate, the internal buffer can store data for up to 1 s per run.

The acquisition parameters were adapted to the purpose of each measurement. For the n-i-p detector operated with the UOW system, a sampling period of 20 ms was used to perform dose response measurements over multiple pulses.

The CSC and the p-i-n detectors were read out with the TetrAMM system to conduct studies with higher temporal resolution. Signals were acquired with a sampling period of 10 μs, allowing reconstruction of the beam time structure within a 0.1-s acquisition window. A limitation of the acquisition chain is that the minimum achievable sampling period is longer than the typical pulsewidth (about 3 μs), which prevents an accurate reconstruction of the individual pulse shape. However, this does not affect the determination of detector sensitivity, which is based on the total collected charge, and mainly impacts future developments aimed at pulse-resolved dosimetry.

Although two different acquisition approaches were used due to instrumental constraints, all results are expressed in terms of collected charge, ensuring a consistent comparison of sensitivity across detector architectures and irradiation modalities.

Both systems were interfaced with a LabVIEW program for data acquisition, real-time visualization, and data storage for later analysis.

III. Dose Response Linearity and Sensitivity

The response of each detector was evaluated in terms of collected charge as a function of delivered dose, with the aim of determining dose linearity and sensitivity. These quantities were chosen as the main figures of merit, as they directly reflect charge generation and collection efficiency and their dependence on detector architecture and internal electric field.

For the n-i-p detectors, measurements were performed by varying the delivered dose. In contrast, for the p-i-n and CSC detectors, the output current was recorded over a fixed time window while varying the beam dose rate. These two analysis approaches arise from the fact that, with the TetrAMM electronics, a measurable signal was obtained only when fast sampling was used. In both cases, the total collected charge was calculated by integrating the current trace above the baseline. Repeated measurements (at least three per dose point) were performed to assess reproducibility. The average collected charge was used as the reference value, and the associated uncertainty was estimated as the standard deviation of the repeated acquisitions.

Detector sensitivity was defined as the slope of the charge dose calibration curve obtained by linear regression of the measured data. This definition allows a direct comparison across different detector architectures and irradiation modalities. Dose response linearity was quantified using the coefficient of determination (R^2) of the linear fit, with values close to unity indicating a strong proportionality between collected charge and absorbed dose.

IV. Influence of Bias Voltage

All detectors investigated in this work were designed to operate in unbiased mode (0 V), which is the preferred configuration for flexible and potentially large area detectors, as it simplifies the readout electronics and improves the electrical safety of wearable devices.

To further study the role of the internal electric field in charge collection and to evaluate possible improvements in sensitivity and signal-to-noise ratio (SNR) under reverse bias, additional measurements were performed by repeating the full set of acquisitions at different bias voltages (0, 1, 3, and 5 V). Owing to time constraints, these tests were carried out only on the n-i-p detector, which is used here as a reference structure to examine the effect of an applied electric field.

The dependence of sensitivity on the applied bias was described using an inverted exponential function (as discussed in [15])

$$S = p_0 \cdot \left(1 - p_1 \cdot e^{-p_2 V}\right) \quad (1)$$

where S is the detector sensitivity at bias voltage V, and p_0, p_1, and p_2 are fitting parameters that represent the saturation sensitivity, a scaling factor, and the voltage dependence, respectively.

V. Results

Only pixels meeting predefined stability and performance criteria, as determined by preliminary electrical screening,

TABLE I

AVERAGE SENSITIVITY OF THE THREE DETECTOR ARCHITECTURES UNDER FFF 6-MV PHOTON BEAM IRRADIATION AT 0-V BIAS. VALUES REPRESENT THE MEAN FOR THE GIVEN NUMBER OF PIXELS (N). THE CORRESPONDING SENSITIVITY DATA ARE REPORTED IN TABLES VI AND VII

Sensitivity - Photon beams					
Detector	**Pixel size [mm^2]**	**Intrinsic layer [μm]**	**N**	**Photon beam**	**Sensitivity [pC/cGy]**
n-i-p	2.5 × 2.5	2.5	4	6 MV FFF 6 MV 10 MV	0.045 ± 0.003 0.041 ± 0.005 0.042 ± 0.004
CSC	2 × 2 5 × 5	5.0 5.0	2 2	FFF 6 MV FFF 6 MV	8.205 ± 0.007 17.9 ± 0.4
p-i-n	2 × 2	0.4	7	FFF 6 MV	6.9 ± 0.3

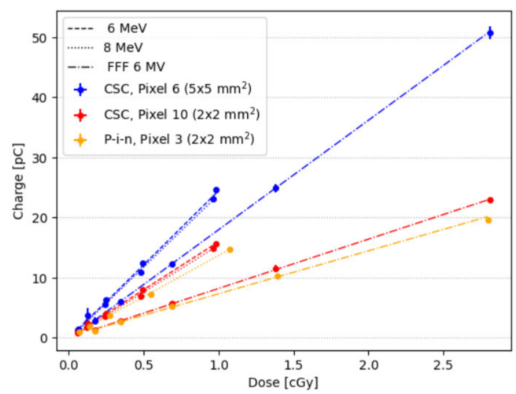

Fig. 6. Charge–dose curves obtained for pixels 6 and 10 of the CSC detector and pixel 3 of the p-i-n device, when irradiated with the FFF 6-MV photon and the 6- and 8-MeV electron beams. Pixel 6 has a size of 5 × 5 mm, while pixels 10 and 3 have an area of 2 × 2 mm.

were included in the dosimetric characterization. The identifier numbers of the pixels used for the acquisitions are reported in Figs. 2–4.

A. Linearity

All three a-Si:H detector architectures, the n-i-p diode, the CSC diode, and the p-i-n diode, exhibit excellent dose response linearity across clinically relevant dose ranges, even when there is no bias voltage applied. Within their tested operating conditions, each device showed a near proportional increase in the collected charge with the delivered dose, as, for example, can be noted from Fig. 6.

The n-i-p's response was highly linear, yielding R^2 coefficients ranging from 0.9996 to 1.0000, from the photon beam measurements. Also, the CSC and p-i-n devices achieved excellent linearity: the CSC pixels yielded $R^2 \approx 0.9987$–1.0000, and the p-i-n pixels showed $R^2 \approx 0.9972$–0.9997, in both photon and electron beam tests. These results indicate that all three architectures can provide the strict linear dose response required for dosimetric applications, up to the highest tested doses and dose rates. All R^2 values are reported in Table VIII.

B. Sensitivity Under Photon Irradiation

When the UOW readout system is used, the detector current is integrated at a low sampling frequency, resulting in nearly constant signal levels whose duration scales with the delivered dose. This acquisition mode is well-suited for integrated dose measurements, as it averages out the contribution of individual beam pulses. Fig. 7 shows an example of signals acquired from pixel 5 of the n-i-p detector at 0-V bias under 6-MV photon beam irradiation, where a clear stepwise increase in collected charge is observed with increasing monitor units (MUs). The corresponding signals exhibit an SNR of approximately 15. Signal-to-noise ratios are reported here as indicative of the measurement quality achieved for each detector under the corresponding acquisition chain. Because different readout systems were used, SNR values should not be interpreted as a strict comparison between detector architectures.

Under FFF 6-MV photon beam irradiation at 0-V bias, the three detector architectures show markedly different sensitivities. The n-i-p device exhibits the lowest response, equal to 41 fC/cGy. In contrast, the CSC and p-i-n detectors produce signals in the pC range, corresponding to values two to three orders of magnitude higher than those of the n-i-p device (see Table I). For both detectors, the SNR exceeds 30 for the smaller pixels and 80 for the larger pixels.

For the n-i-p and p-i-n detectors, the measured responses are tightly clustered around the mean value (with standard deviations of 3 fC/cGy and 0.3 pC/cGy, respectively), while the CSC exhibits minimal variability, with differences of about 4% between large pixels and negligible differences between small pixels (see Table VI).

Additional measurements were performed using the n-i-p detector under 6- and 10-MV photon beams. Relative to the average sensitivity measured with the FFF 6-MV beam, the corresponding values differ by 10% and 2%, respectively (see Table I).

C. Sensitivity Under Electron Irradiation

For electron beam irradiation, measurements were performed on CSC and p-i-n detectors, while the n-i-p device was not evaluated in this configuration.

The CSC detector was exposed to clinical 6- and 8-MeV electron beams at 0-V bias. Data were acquired using the TetrAMM picoammeter with a shorter sampling period, allowing the pulsed structure of the beam to be resolved, as shown in Fig. 8. As the dose rate increases, a corresponding increase in the number of pulses is observed. The CSC detector exhibits a stable response in the pC/cGy range (see Table II). A modest reduction in sensitivity of about 4% is observed at the higher electron energy for both pixel sizes, consistent with a lower dose deposition in the active layer at 8 MeV. The uniformity

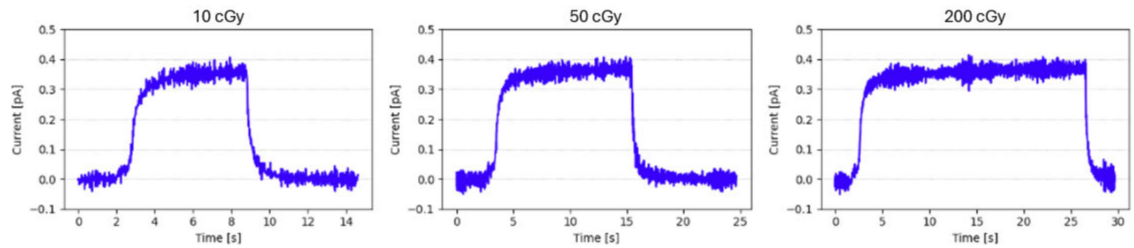

Fig. 7. Signals from pixel 5 of the n-i-p detector, acquired by varying the dose value of the 6-MV photon beam and setting 0-V bias voltage.

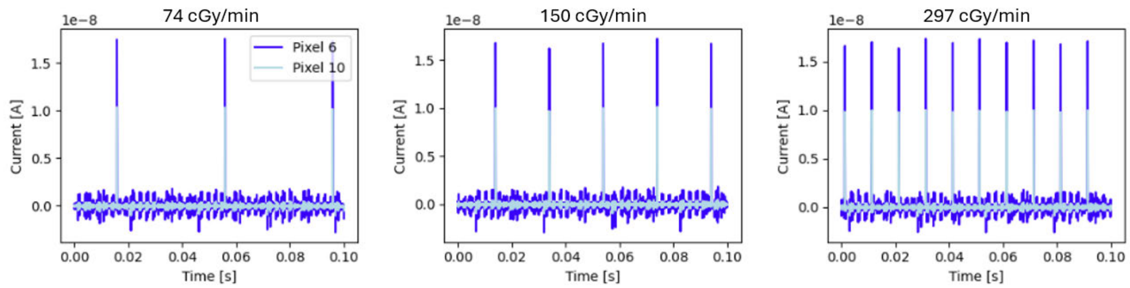

Fig. 8. Signals from pixel 6 (5 × 5 mm) and pixel 10 (2 × 2 mm) of the CSC detector, acquired by varying the dose rate of the 6-MeV electron beam.

TABLE II
AVERAGE SENSITIVITY OF CSC AND p-i-n DETECTORS UNDER ELECTRON BEAM IRRADIATION AT 0-V BIAS. VALUES REPRESENT THE MEAN FOR THE GIVEN NUMBER OF PIXELS (N). THE CORRESPONDING SENSITIVITY DATA ARE REPORTED IN TABLE IV

Sensitivity – Electron beams					
Detector	**Pixel size [mm^2]**	**Intrinsic layer [μm]**	**N**	**Electron beam**	**Sensitivity [pC/cGy]**
CSC	2 × 2	5.0	2	6 MeV	15.92 ± 0.09
				8 MeV	15.35 ± 0.07
	5 × 5	5.0	2	6 MeV	24.7 ± 0.6
				8 MeV	23.7 ± 0.6
p-i-n	2 × 2	0.4	4	8 MeV	13.7 ± 0.7

across pixels under electron irradiation closely follows the photon results: the two smaller pixels show nearly identical sensitivity (within ±0.1 pC/cGy), while the larger pixels differ by about 3% (see Table IV).

The p-i-n detector was tested at 0-V bias using the 8-MeV electron beam. Averaging over all p-i-n pixels yields a mean sensitivity of approximately 13.7 pC/cGy, comparable to that measured for the CSC detector with similar pixel area. Also, in this case, the pixel uniformity agrees with the photon results, showing a percentage difference of 4% (see Table IV). In this case as well, both detectors show SNRs above 30 for the smaller pixels and above 80 for the larger pixels.

When comparing different irradiation modalities, the collected charge per unit dose is higher for 6-MeV electrons than for 6-MV photons in the same detector, with an increase of roughly a factor of 1.5–2. This behavior reflects the higher dose deposition in the active volume by electron beams. Despite these differences in absolute sensitivity, a linear dose response is observed under all conditions.

D. Bias Voltage Scan

As expected, the application of an external bias has a clear impact on detector sensitivity. The average sensitivity increases from 0.045 pC/cGy at 0 V to 0.243 pC/cGy at 5 V (see Table III), corresponding to an enhancement by more than a factor of five. This trend reflects the increase in the electric field across the intrinsic layer. Moreover, the n-i-p detector

TABLE III
AVERAGE SENSITIVITY OF THE n-i-p DETECTOR UNDER 6-MV PHOTON BEAM IRRADIATION AT DIFFERENT BIAS VOLTAGES. VALUES ARE MEAN ± STANDARD DEVIATION FOR THE FOUR PIXELS WITH A 2.5 mm × 2.5 mm SIZE. THE SENSITIVITY DATA OF THE PIXELS USED TO CALCULATE THE AVERAGES ARE PRESENT IN TABLE V

Sensitivity n-i-p detector - 6 MV photon beam	
Bias Voltage	**Sensitivity [pC/cGy]**
0 V	0.045 ± 0.003
1 V	0.109 ± 0.005
3 V	0.189 ± 0.008
5 V	0.243 ± 0.007

maintains good dose linearity over the full investigated bias range, with R^2 values between 0.986 and 1.000 (see Table V). This confirms that the increase in sensitivity with bias does not compromise the linear response of the device. For example, this can be observed in Fig. 9, which shows the charge curves acquired with pixel 5 of the n-i-p detector at different bias voltages.

All n-i-p pixels share the same geometry and show comparable sensitivities, with a maximum pixel-to-pixel standard deviation of 8 fC/cGy observed at 3-V bias (see Table V).

Fig. 10 shows the sensitivity as a function of the applied bias voltage for the four n-i-p pixels, together with the fits

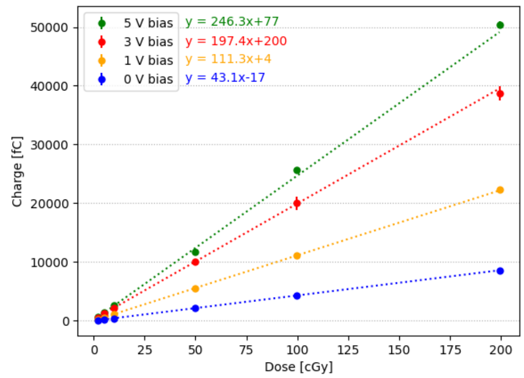

Fig. 9. Charge values acquired with pixel 5 of the n-i-p detector as a function of dose for the 6-MV photon beam measurements performed with different bias voltages.

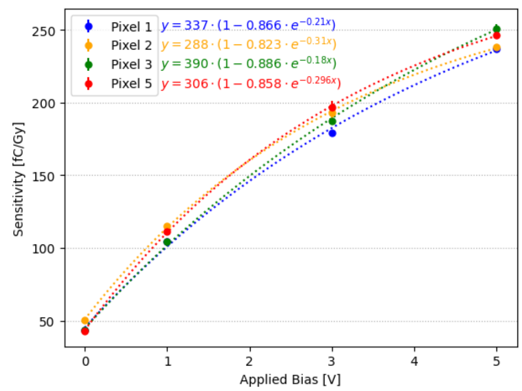

Fig. 10. Sensitivities of the n-i-p detector pixels as a function of the applied bias voltage. The dashed lines represent the trends obtained by fitting the data using (1). In the legend for each pixel, the fit parameters are reported.

obtained using (1). A rapid increase in sensitivity is observed at low bias, followed by a gradual saturation at higher voltages.

Regarding the SNR, values increase from about 15 at 0 V to approximately 86 at 3 V, indicating a significant improvement in signal quality with increasing electric field. At 5 V, the SNR decreases to about 68. This reduction is attributed to increased electronic noise, likely related to contact resistance and to higher leakage contributions at elevated bias.

VI. Discussion

A. Overview of the Experimental Trends

The experimental results presented in this work show a clear and systematic dependence of sensitivity at zero bias on detector architecture. Under identical clinical irradiation conditions, the three flexible a-Si:H devices investigated, namely, the n-i-p, CSC, and very thin p-i-n detectors, exhibit sensitivities that differ by more than two orders of magnitude. This behavior is consistently observed for both photon and electron irradiation and for different pixel sizes, and is further supported by the bias voltage scan performed on the n-i-p detector.

The CSC and p-i-n detectors operate in the pC/cGy range, while the n-i-p detector remains in the fC/cGy range. The reproducibility of these results across multiple pixels and irradiation conditions indicates that the observed differences are intrinsic to the detector design, rather than arising from local defects, measurement artifacts, or readout effects.

These results indicate that, for flexible a-Si:H dosimeters, sensitivity is not determined solely by the active volume. Instead, it is strongly influenced by the internal electric field distribution, charge transport, and charge extraction processes, which are governed by the thickness of the intrinsic layer and the contact design [4], [5].

B. Charge Collection Limited by the Electric Field in n-i-p Devices

The much lower sensitivity observed at zero bias in the conventional n-i-p detector can be explained in terms of charge collection limited by the electric field. In a-Si:H, carrier transport is strongly influenced by trapping and recombination processes associated with the high density of localized states [4]. When the electric field is weak, a significant fraction of the radiation-induced charges recombines before reaching the electrodes, leading to poor charge collection.

The bias voltage scan performed on the n-i-p detector provides direct experimental evidence of this behavior. The increase in sensitivity with applied reverse bias reflects the stronger electric field across the intrinsic layer, which increases charge drift velocity, shortens transit time, and reduces trapping losses. The rapid rise in sensitivity at low bias, followed by a gradual saturation at higher voltages, is consistent with a transition from a regime dominated by recombination to one limited by charge collection, in agreement with the model described in [15].

These results show that the low sensitivity at zero bias in the n-i-p device arises from inefficient charge extraction rather than from limited charge generation. Even a modest applied bias is sufficient to significantly improve charge collection, demonstrating that the electric field is the main limiting factor in this device architecture.

C. Role of Charge Selective Contacts in CSC Devices

The CSC architecture adopts a contact scheme that differs from conventional designs, replacing doped layers with transition metal oxide contacts that selectively extract charge carriers. This approach directly affects both the internal electric field distribution and the recombination processes at the interfaces.

Unlike heavily doped p and n layers, which can introduce a high density of defect states and enhance interfacial recombination [5], MoO_x and TiO_2 layers allow selective extraction of holes and electrons while limiting minority charge injection. In addition, their large work function offsets and the resulting band alignment at the oxide and semiconductor interfaces can promote the formation of a strong built-in electric field across the intrinsic layer, even in the absence of an external bias [7]. Similar dopant-free contact concepts have been extensively investigated in photovoltaic devices as an effective strategy to improve charge selectivity and reduce recombination losses, providing a useful physical framework for understanding charge extraction in CSC devices [6].

The high sensitivity observed at zero bias in CSC detectors under both photon and electron irradiation is consistent with this interpretation. Efficient charge extraction in the absence of an external bias indicates that the internal electric field and interface properties are sufficient to drive charge separation and transport, leading to a marked improvement in charge collection compared to conventional n-i-p structures.

The excellent uniformity across pixels observed in CSC detectors further supports the conclusion that this enhancement is intrinsic to the contact scheme and not dominated by localized or pixel-dependent effects.

D. Effect of Intrinsic Layer Thickness: Performance of Very Thin p-i-n Devices

A second key result of this study is that the very thin p-i-n device, despite the strongly reduced thickness of its intrinsic layer, shows a sensitivity at zero bias comparable to that of much thicker CSC devices and several orders of magnitude higher than that of the thick n-i-p detector.

This result shows that, in a-Si:H dosimeters, sensitivity does not scale simply with the active volume. For a given built-in potential, reducing the intrinsic layer thickness increases the average electric field, leading to higher charge drift velocities and shorter transit times. As a consequence, the probability of trapping and recombination before charge collection is reduced [4]. In addition, thinner intrinsic layers shorten the distance charges must travel, further limiting the impact of localized states and transport dispersion. In this regime, the gain in collection efficiency can compensate for the reduced charge generation associated with the smaller active volume, increasing the sensitivity. The performance of the very thin p-i-n device, therefore, indicates that, even in the absence of an external bias, the electric field and charge transport conditions can be sufficient to ensure efficient charge collection. This supports the interpretation that internal electric field strength and charge transport play a dominant role in determining sensitivity at zero bias in flexible a-Si:H detectors.

E. Consistency Across Radiation Modalities and Implications for Device Design

The architectural trends identified in this study are observed under both photon and electron irradiation. In addition, the variations in sensitivity with beam energy follow a behavior that is physically consistent with differences in local dose deposition. This consistency indicates that the improved performance of CSC and very thin p-i-n detectors is governed by intrinsic device properties, rather than by effects specific to a given radiation modality.

Taken together, these results show that suitable contact design and control of the intrinsic layer thickness provide an effective way to overcome the charge collection limitations observed in conventional n-i-p devices, enabling high sensitivity operation without external bias in flexible a-Si:H dosimeters [2], [3].

From a device design perspective, these findings suggest that future flexible dosimeters should focus on architectures that enhance the internal electric field and reduce recombination at the interfaces, rather than relying only on increasing the active volume. This approach is particularly relevant for applications that require lightweight and conformable detectors operating without external bias, such as surface and transmission dosimetry in advanced RT.

VII. Conclusion

In this work, a comparative characterization of three flexible a-Si:H detector architectures was performed under clinical photon and electron beams, highlighting the central role of device design in determining sensitivity at zero bias. All detectors showed excellent dose linearity over clinically relevant dose ranges and irradiation conditions, confirming their suitability for quantitative dosimetry. However, their absolute sensitivities differed by more than two orders of magnitude, demonstrating that sensitivity in a-Si:H dosimeters is not set by the active volume alone but is strongly governed by intrinsic layer thickness, contact design, and the resulting internal electric field.

CSC and very thin p-i-n detectors reached sensitivities in the pC/cGy range under unbiased operation, exceeding that of the conventional n-i-p diode by two to three orders of magnitude. Together with the bias scan performed on the n-i-p device, these results show that conventional architectures are limited by inefficient charge extraction at zero bias, while CSC and very thin p-i-n designs achieve efficient charge separation and collection without external polarization.

All detector types showed reasonably good uniformity across the selected working pixels of the same size, suggesting an acceptable level of reproducibility within the currently available fabrication process. In CSC devices, however, the scaling of sensitivity with pixel area is weaker than expected from simple geometric considerations, suggesting the presence of residual field nonuniformities or partial charge loss in larger pixels. This observation indicates that electrode layout and segmentation remain important parameters for further optimization.

From a design and application standpoint, these findings identify CSC and thin-film p-i-n detectors as strong candidates for flexible, large-area, and bias-free dosimetry, where high sensitivity and minimal system complexity are required. These results suggest two favorable design directions for zero-bias operation, namely, the use of CSCs and the reduction of intrinsic layer thickness. Their combined implementation may represent a promising strategy for future device optimization.

Future work will focus on refining contact design and intrinsic layer thickness to further enhance charge collection without bias, improving charge transport uniformity over large areas, and integrating fast and low-noise readout electronics. These developments are expected to enable flexible a-Si:H dosimeters suitable for real-time operation in advanced RT applications, including high-dose-rate FFF and emerging FLASH beams.

Appendix

This appendix contains summary tables of the sensitivity and linearity data from which the average values shown in Section V were extracted.

TABLE IV
PIXEL-BY-PIXEL SENSITIVITY OF THE CSC AND p-i-n DETECTORS UNDER 6- AND 8-MeV ELECTRON BEAMS IRRADIATION (0-V BIAS)

Electron beams				
Detector	**Pixel**	**Pixel size [mm×mm]**	**Beam**	**Sensitivity [pC/cGy]**
CSC	6	5×5	6 MeV	25.1 ± 0.2
	9		6 MeV	24.2 ± 0.2
	10	2×2	6 MeV	15.98 ± 0.14
	11		6 MeV	15.85 ± 0.15
	6	5×5	8 MeV	24.1 ± 0.4
	9		8 MeV	23.3 ± 0.4
	10	2×2	8 MeV	15.4 ± 0.3
	11		8 MeV	15.3 ± 0.3
p-i-n	1	2×2	8 MeV	14.71 ± 0.08
	3		8 MeV	13.70 ± 0.07
	4		8 MeV	13.09 ± 0.05
	5		8 MeV	13.26 ± 0.06

TABLE V
PIXEL-BY-PIXEL SENSITIVITY AND DOSE-RESPONSE LINEARITY OF THE n-i-p DETECTOR WHEN IRRADIATED WITH THE 6-MV PHOTON BEAM, AT DIFFERENT BIAS VOLTAGES. ALL THE PIXELS HAVE THE SAME DIMENSIONS OF 2.5 × 2.5 mm

N-i-p detector - 6 MV Photon beam			
Bias Voltage	**Pixel**	**Sensitivity [fC/cGy]**	**R^2**
0 V	1	43.7 ± 0.2	1.0000
	2	50.4 ± 0.4	0.9998
	3	43.5 ± 0.3	0.9999
	5	43.1 ± 0.2	0.9999
1 V	1	104.3 ± 0.6	1.0000
	2	115.1 ± 0.6	1.0000
	3	104.3 ± 0.5	0.9998
	5	111.3 ± 0.5	0.9999
3 V	1	179.5 ± 1.6	0.9998
	2	193 ± 5	0.9966
	3	187.1 ± 1.4	0.9862
	5	197 ± 4	0.9994
5 V	1	237 ± 2	0.9966
	2	238 ± 2	0.9994
	3	251 ± 3	0.9960
	5	246.2 ± 1.7	0.9984

TABLE VI
PIXEL-BY-PIXEL SENSITIVITY OF THE n-i-p, CSC, AND p-i-n DETECTORS UNDER FFF 6-MV PHOTON BEAM IRRADIATION (0-V BIAS)

FFF 6 MV Photon beam			
Detector	**Pixel**	**Pixel size [mm×mm]**	**Sensitivity [pC/cGy]**
n-i-p	1	2.5×2.5	0.03617 ± 0.00018
	2		0.04753 ± 0.00012
	3		0.04190 ± 0.00007
	5		0.0392 ± 0.0003
CSC	6	5×5	18.23 ± 0.05
	9		17.60 ± 0.05
	10	2×2	8.20 ± 0.05
	11		8.21 ± 0.04
p-i-n	3	2×2	7.15 ± 0.14
	4		7.18 ± 0.18
	5		6.86 ± 0.19
	8		6.60 ± 0.12
	11		6.76 ± 0.13
	12		6.29 ± 0.13
	13		7.15 ± 0.14

TABLE VII
PIXEL-BY-PIXEL SENSITIVITY OF THE N-I-P DETECTOR AT 0 V BIAS VOLTAGE, UNDER 6- AND 10-MV PHOTON BEAMS' IRRADIATION. ALL THE PIXELS HAVE THE SAME DIMENSIONS OF 2.5 × 2.5 mm

Photon beam	Detector	Pixel	Sensitivity [fC/cGy]
6 MV	n-i-p	1	43.7 ± 0.2
		2	50.4 ± 0.4
		3	43.5 ± 0.3
		5	43.1 ± 0.2
10 MV	n-i-p	1	37.4 ± 0.4
		2	47.6 ± 0.3
		3	41.7 ± 0.3
		5	41.75 ± 0.04

TABLE VIII
DOSE RESPONSE LINEARITY AT 0-V BIAS FOR THE MEASURED DETECTORS UNDER THE INVESTIGATED BEAM CONDITIONS. WHERE PIXELS YIELDED INDISTINGUISHABLE R^2 VALUES, THEY ARE REPORTED TOGETHER

Detector	Beam	Pixel	R^2
n-i-p	Photon 6 MV	1	1.0000
	Photon 6 MV	2	0.9998
	Photon 6 MV	3	0.9996
	Photon 6 MV	5	0.9999
	Photon 6 MV FFF	1,2,3	0.9999
	Photon 6 MV FFF	5	0.9997
	Photon 10 MV	1	0.9996
	Photon 10 MV	2	0.9998
	Photon 10 MV	3	0.9999
	Photon 10 MV	5	1.0000
CSC	Photon 6 MV FFF	6,9	1.0000
	Photon 6 MV FFF	10,11	0.9999
	Electron 6 MeV	6,9,10,11	0.9987
	Electron 8 MeV	6,9,11	0.9992
	Electron 8 MeV	10	0.9991
p-i-n	Photon 6 MV FFF	3	0.9983
	Photon 6 MV FFF	4	0.9972
	Photon 6 MV FFF	5	0.9978
	Photon 6 MV FFF	8	0.9980
	Photon 6 MV FFF	11	0.9983
	Photon 6 MV FFF	12,13	0.9982
	Electron 8 MeV	1	0.9992
	Electron 8 MeV	3	0.9993
	Electron 8 MeV	4	0.9997
	Electron 8 MeV	5	0.9995

ACKNOWLEDGMENT

M. Ponzecchi and C. Talamonti are with the Dipartimento di Scienze Biomediche Sperimentali e Cliniche "Mario Serio," Università degli Studi di Firenze, 50134 Florence, Italy, and also with INFN sezione di Firenze, 50019 Sesto Fiorentino,, Italy (e-mail: ponzecchimarta@gmail.com; cinzia.talamonti@unifi.it).

K. Kanxheri is with INFN sezione di Perugia, 06123 Perugia, Italy, and also with the Dipartimento di Fisica e Geologia, Università degli Studi di Perugia, 06123 Perugia, Italy (e-mail: keida.kanxheri@pg.infn.it).

L. Servoli is with INFN Sezione di Perugia, 06123 Perugia, Italy (e-mail: leonello.servoli@pg.infn.it).

M. V. Rossi and E. Gazzera are with the Dipartimento di Scienze Biomediche Sperimentali e Cliniche “Mario Serio,” Università degli Studi di Florence, 50134 Florence, Italy.

G. Insero and S. Pallotta are with the Dipartimento di Scienze Biomediche Sperimentali e Cliniche “Mario Serio,” Università degli Studi di Florence, 50134 Florence, Italy, and also with INFN Sezione di Florence, 50019 Sesto Fiorentino, Italy.

M. Fabi, C. Grimani, and M. Villani are with the Dipartimento di Scienze Pure e Applicate (DiSPeA), Università di Urbino Carlo Bo, 61029 Urbino, Italy, and also with INFN Sezione di Florence, 50019 Sesto Fiorentino, Italy.

F. Sabbatini is with INFN Sezione di Florence, 50019 Sesto Fiorentino, Italy.

S. Aziz, L. Calcagnile, A. P. Caricato, M. Martino, G. Maruccio, A. G. Monteduro, G. Quarta, and S. Rizzato are with INFN Sezione di Lecce, 73100 Lecce, Italy, and also with the Department of Mathematics and Physics “Ennio de Giorgi,” University of Salento, 73100 Lecce, Italy.

R. Catalano, G. A. P. Cirrone, G. Cuttone, M. Guarrera, and G. Petringa are with the INFN Laboratori Nazionali del Sud, 95123 Catania, Italy.

L. Frontini, V. Liberali, and A. Stabile are with INFN Sezione di Milan, 20133 Milan, Italy, and also with the Dipartimento di Fisica, Università degli Studi di Milan, 20133 Milan, Italy.

M. M. S. Vasquez is with the INFN Sezione di Milan, 20133 Milan, Italy.

F. Cittadini and T. Croci are with INFN Sezione di Perugia, 06123 Perugia, Italy, and also with the Dipartimento di Fisica e Astronomia, Università di Padua, 35131 Padua, Italy.

M. Ionica, M. Menichelli, A. Morozzi, and F. Peverini are with INFN Sezione di Perugia, 06123 Perugia, Italy.

D. Passeri is with INFN Sezione di Perugia, 06123 Perugia, Italy, and also with the Dipartimento di Ingegneria, Università degli studi di Perugia, 06125 Perugia, Italy.

P. Placidi is with INFN Sezione di Perugia, 06123 Perugia, Italy, and also with the Dipartimento di Ingegneria, Università degli studi di Perugia, 06125 Perugia, Italy.

M. Pedio is with INFN Sezione di Perugia, 06123 Perugia, Italy, and also with the CNR Istituto Officina dei Materiali (IOM), 06123 Perugia, Italy.

N. Zema is with INFN Sezione di Perugia, 06123 Perugia, Italy, and also with the CNR Istituto struttura della Materia, 00133 Rome, Italy.

D. Caputo, G. de Cesare, and N. Lovecchio are with INFN, Rome, Italy, and also with the Department of Information Engineering, Electronics and Telecommunications, Sapienza University of Rome, 00184 Rome, Italy.

A. Nascetti is with INFN, Rome, Italy, and also with the Scuola di Ingegneria Aerospaziale Sapienza University of Rome, 00138 Rome, Italy.

M. Cazzanelli, H. Hasnaoui, M. Polo, and A. Quaranta are with INFN TIFPA c/o Dipartimento di fisica dell’Università di Trento, 38123 Povo, Trento, Italy.

D. Calvo, R. Cirio, P. De Remigis, G. Mazza, and R. J. Wheadon are with the INFN sezione di Turin, 10125 Turin, Italy.

F. Lenta is with INFN Sezione di Turin, 10125 Turin, Italy, and also with the Politecnico di Turin, 10129 Turin, Italy.

S. Dunand, G. Konstantinou, N. Wyrsch, and L. Barraud are with the Ecole Polytechnique Fédérale de Lausanne (EPFL), Photovoltaics and Thin-Film Electronics Laboratory (PV-Lab), 2000 Neuchâtel, Switzerland.

M. Large and M. Petasecca are with the Center for Medical Radiation Physics, University of Wollongong, Wollongong, NSW 2522, Australia.

A. Bashiri is with the Center for Medical Radiation Physics, University of Wollongong, Wollongong, NSW 2522, Australia, and also with the Faculty of Arts and Sciences, Department of Physics, Najran University, Najran 1988, Saudi Arabia.

REFERENCES

[1] C. Garibaldi et al., “Recent advances in radiation oncology,” *ecancermedicalscience*, vol. 11, p. 785, Nov. 2017, doi: 10.3332/ecancer.2017.785.

[2] M. Menichelli et al., “Development of thin hydrogenated amorphous silicon detectors on a flexible substrate,” 2022, *arXiv:2211.17114*.

[3] M. Menichelli et al., “Characterization of hydrogenated amorphous silicon sensors on polyimide flexible substrate,” *IEEE Sensors J.*, vol. 24, no. 8, pp. 12466–12471, Apr. 2024, doi: 10.1109/JSEN.2024.3359861.

[4] R. A. Street, *Hydrogenated Amorphous Silicon*. Cambridge, U.K.: Cambridge Univ. Press, 1991.

[5] J. Balent, F. Smole, M. Topic, and J. Krc, “Nalysis of effects of dangling-bond defects in doped a-Si: H layers in heterojunction silicon solar cells with different electron affinities of ITO contacts,” *J. Microelectron. Electron. Compon. Mater.*, vol. 52, no. 2, pp. 129–142, 2022, doi: 10.33180/InfMIDEM2022.206.

[6] J. Bullock et al., “Efficient silicon solar cells with dopant-free asymmetric heterocontacts,” *Nature Energy*, vol. 1, no. 3, Jan. 2016, Art. no. 15031, doi: 10.1038/nenergy.2015.31.

[7] A. Klein, “Energy band alignment at interfaces of semiconducting oxides,” *Thin Solid Films*, vol. 520, no. 10, pp. 3721–3728, 2012.

[8] D. Caputo, N. Lovecchio, G. de Cesare, and M. Cavagnaro, “Amorphous silicon diodes as temperature sensors in microwave thermal ablation applications: An initial assessment,” *IEEE Sensors J.*, vol. 24, no. 17, pp. 27198–27204, Sep. 2024, doi: 10.1109/JSEN.2024.3431211.

[9] F. Di Martino et al., “Architecture, flexibility and performance of a special electron linac dedicated to flash radiotherapy research: ElectronFlash with a triode gun of the centro pisano flash radiotherapy (CPFR),” *Frontiers Phys.*, vol. 11, Nov. 2023, Art. no. 1268310, doi: 10.3389/fphy.2023.1268310.

[10] T. Isidori et al., “Performance of a low gain avalanche detector in a medical linac and characterisation of the beam profile,” *Phys. Med. Biol.*, vol. 66, no. 13, Jul. 2021, Art. no. 135002, doi: 10.1088/1361-6560/ac0587.

[11] Linax Technologies Ltd., *Linax*. Accessed: Nov. 2025. [Online]. Available: https://linax.ca/

[12] *International Atomic Energy Agency, Absorbed Dose Determination in External Beam Radiotherapy: An International Code of Practice for Dosimetry Based on Standards of Absorbed Dose to Water*, IAEA, Vienna, Austria, 2000.

[13] I. Fuduli et al., “A comparative analysis of multichannel data acquisition systems for quality assurance in external beam radiation therapy,” *J. Instrum.*, vol. 9, no. 6, Jun. 2014, Art. no. T06003, doi: 10.1088/1748-0221/9/06/t06003.

[14] *CAEN ELS, TetraMM—Multi-Channel Digital Multimeter*. Accessed: Nov. 2025. [Online]. Available: https://www.caenels.com/product/tetramm/

[15] M. J. Large et al., “Characterization of a flexible a-Si:H detector for in vivo dosimetry in therapeutic X-ray beams,” *Med. Phys.*, vol. 51, no. 6, pp. 4489–4503, Mar. 2024, doi: 10.1002/mp.17013.

Open Access funding provided by ‘Universita Degli Studi di Firenze’ within the CRUI CARE Agreement